Journal of Electronic Materials (2024) 53:5083–5091
https://doi.org/10.1007/s11664-024-11127-4

28TH INTERNATIONAL CONFERENCE ON NUCLEAR TRACKS AND RADIATION MEASUREMENTS

Tailoring the Physiochemical Properties of Sn-Doped V_2O_5 Using SHI Irradiation

Ashish K. Kumawat[1] · Kriti Kumari[1] · Satyapal S. Rathore[2] · Indra Sulania[3] · Rashi Nathawat[1]

Received: 29 December 2023 / Accepted: 17 April 2024 / Published online: 21 May 2024

Abstract
When subjected to swift heavy ion (SHI) irradiation, a lattice acquires sufficient energy to induce desirable flaws in the material. In this study, the physiochemical properties of Sn-doped V_2O_5 (SVO) synthesized by a sol–gel process were thoroughly examined following irradiation with Ni^{+11} ions at 150 MeV energy and fluence of 2.51×10^{11} ions/cm^2. The successful doping of Sn in V_2O_5 was confirmed by an increase in tensile strain, as revealed by the x-ray diffraction (XRD) spectrum, and the presence of characteristic peaks of constituent elements detected in the energy-dispersive x-ray (EDX) spectrum. Atomic force microscopy (AFM) and field-emission scanning microscopy (FESEM) images revealed an increase in surface roughness and transformation to an amorphous state, respectively. The Tauc plot indicated an increase in the electronic bandgap post-irradiation. Fourier transform infrared (FTIR) spectroscopy analysis revealed a peak shift in the fingerprint region indicating a change in the vibrational energy of the involved molecular bonds. These findings highlight the potential of SHI irradiation for the tuning of material properties, paving the way for a wide range of functional applications of the material.

Keywords Sol–gel technique · SHI irradiation · Thermal spike · Bond weakening model

Introduction

Swift heavy ion (SHI) irradiation is a potent technique for inducing controlled modifications on the atomic scale. In this technique, ions having mass equal to or greater than carbon, propelled at a comparable velocity of an electron in Bohr orbit (10^6 m/s), are directed onto the material. Expressed in units of energy (MeV/amu), SHI experiences energy loss (dE/dx) along its trajectory upon interaction with the material.[1] Elastic collision with the target dominates for ions having an energy of about 1 KeV/amu, which results in the scattering of ions without substantial energy dissipation.[2] Inelastic collision is more prevalent for ions having energy of about 1 MeV/amu or more, wherein a highly charged projectile energizes electrons in its path, causing excitation (10^{-17} to 10^{-15} s) and ionization (10^{-15} to 10^{-13} s) of the electrons. This encounter results in disruption of the charge distribution, as the energetic electrons are excited away from the ion's path, leaving behind a localized region of a positive core. These occurrences serve as the foundation for the ionic spike model. The accumulation of like charges within this region leads to a robust repulsion, compelling the ions to swiftly disperse in a coordinated movement, away from the centre, resulting in a Coulomb explosion.[3] Soon these separated charges recombine, and the spatial charge neutrality is restored.[4] Nevertheless, a few electrons persist in the excited state, engaging in faster energy exchange with comparable masses, establishing a temperature deferential between electrons and lattice.[5] In response to the changes in atomic interlinkage due to highly excited electrons, the crystal lattice undergoes relaxation ($< 10^{-12}$ s). The energy is transmitted to the lattice via electron–phonon interaction within a very short time frame ($< 10^{-13}$ s), which elevates the lattice temperature locally.[6,7] This increase in temperature is a key

✉ Satyapal S. Rathore
satyapal03@gmail.com

✉ Rashi Nathawat
rashi.nathawat@gmail.com

[1] Functional Ceramic and Smart Material Lab, Department of Physics, Manipal University Jaipur, Jaipur 303007, India

[2] Department of Physics, Cluster University Jammu, Jammu 18001, India

[3] Inter-University Accelerator Centre, New Delhi 110067, India

aspect of the thermal spike model.[8] However, this model neglects the alterations that occur during lattice relaxation. In describing the course of lattice relaxation, two additional models have received relatively less attention in subsequent discussion of SHI irradiation on the material. When electrons move to a higher energy level, this may disrupt the balance of forces within the bond, making it more susceptible to breaking. The bond-weakening model articulates the potential impact of electronic excitation on bond strength, offering insights into how this phenomenon can contribute to structural modifications in the material.[1,9] As outlined by the self-trapping exciton model, the excitons formed by excited electrons and holes left behind possess localized energy, capable of breaking bonds.[10]

The selection of ion species, energy, and fluence dictates the irradiation effect on the target. Different ion species having distinct masses, charges, and electronic structures interact uniquely with the target. The energy of the ions dictates their penetration depth. Low-energy ions may interact primarily with the surface, inducing surface modifications whereas highly energetic ions can penetrate deeper, causing bulk modifications and potential structural changes. Fluence is a measure of ions incident per unit area. Dose-dependent effects may include defect density, phase transitions, or changes in material properties.[11–14] Some mainstream applications of SHI research include conducting bulk material testing, simulating cosmic radiation effects, exploring SHI-induced sputtering, and developing ion track nanotechnology.[2,15]

The versatility of oxygen in its ability to combine with various metals and nonmetals is enormous, and the resulting compounds are called oxides. V_2O_5 is a transition metal oxide composed of metal vanadium (V) and oxygen (O). These compounds exhibit semiconductor behaviour and have earned favor among scientists for their wide range of applications, for example, in electrochromic devices,[16,17] catalysis,[18] energy storage,[19] and gas sensors.[20,21] Doping of V_2O_5, wherein the intentional incorporation of foreign elements enhances their properties and behaviour, can bring about significant changes to their chemical, optical, and electrical properties.[17,22–24] Employing SHI irradiation enables us to amend the properties of doped oxides.[24,25]

Over the years, Sn-doped V_2O_5 (SVO) has attracted attention for its commendable performance as an ammonia gas sensor[26,27] and for its application in lithium-ion batteries (LIBs).[28–30] Since then, several methods have been adopted to improve the overall efficiency of gas sensors, for example, by manipulating the nanoarchitecture, infusing two-dimensional (2D) nanomaterials, or establishing a hetero-interface,[31] and for LIBs by utilizing silicon as an anode,[32] carbon coatings,[33] and depolarization effects,[34] among others. Aimed at improving performance, this study delves into the influence of Ni^{+11} ion irradiation on enhancing the physiochemical characteristics of SVO. The induced defects such as vacancies, interstitials, or dislocations offer additional sites on SVO for gas molecules to adsorb, thereby increasing gas–surface interaction and enhancing the adsorption capacity of the material. The choice of nickel as an ion species was motivated by its potential as a gas sensor[35,36] and its employment in lithium-ion batteries.[37–39] Furthermore, the highly charged state of Ni^{+11} ions was considered to ensure deeper penetration and more significant interaction with the target.[8]

Experimental

The synthesis of Sn-doped V_2O_5 (SVO) was carried out using the standard sol–gel process. The adoption of this method was in consideration of cost-effectiveness, scalability, and obtaining a homogenous composition, which is crucial for the consistent performance of materials such as electronic devices.[40] Vanadium pentoxide (V_2O_5, ≥ 98%, Sigma-Aldrich), hydrogen peroxide (H_2O_2 30%, Merck), and tin chloride ($SnCl_4$, ≥ 99%, Sigma-Aldrich) were used as precursor materials. The active substance was prepared using deionized (DI) water and 30% hydrogen peroxide (H_2O_2) in a weight ratio of 4:1, respectively. On dissolving 1 g V_2O_5 at 400 rpm, a transparent reddish-brown solution was obtained. For doping, $Sncl_4$ was added at a stoichiometric concentration of 4% under vigorous stirring for 3 h, resulting in a thick, green substance. The solution was left to dry at room temperature. In the next step, the sample was annealed at 450°C for 3 h. The obtained annealed powder and its pallets (1 mm in thickness) were further utilized for characterization and SHI treatment. The SVO pallets were irradiated by a SHI beam of Ni^{+11} for 8 s at 150 MeV and fluence of 2.5×10^{11} ions/cm^2 to maximize the depth of penetration.[41]

To investigate the impact of Ni^{+11} ion beam bombardment onto the SVO having a density of 3.2915 g/cm^3, a stopping and range of ions in matter (SRIM) simulation was conducted. The electronic energy loss $(dE/dx)_e$, which determines the rate of energy loss as ions pass through the material, and the nuclear energy loss $(dE/dx)_n$ determining the dissipation of energy when ions interact with the nucleus were found to be 2.44×10^1 MeV/μm and 3.31×10^{-2} MeV/μm, respectively. The range of the projectile, denoting the distance covered by the ion before coming to rest, was found to be 24.52 μm, indicating easy implantation in a 1-mm-thick pallet. The longitudinal and lateral straggling were identified as 1.09 μm and 1.28 μm, respectively. These findings help us understand the interaction of ions with the target.

The structural, optical, and chemical properties of SVO and irradiated SVO were studied in detail. X-ray diffraction (XRD) with the monochromatic Cu Kα line ($\lambda = 0.154$ nm)

on a Rigaku Ultima IV instrument was carried out for phase identification. Atomic force microscopy (AFM) using a multimode scanning probe microscope system and field-emission electron microscopy (FESEM) using a JEOL JSM-7610F Plus instrument were carried out to explore the surface morphology. UV–visible spectroscopy (Shimadzu UV-2600 spectrophotometer) was utilized to study the optical properties of the material. Fourier transform infrared (FTIR) spectroscopy (Bruker Alpha spectrometer) was used in a spectral range from 500 cm^{-1} to 4000 cm^{-1} for the chemical analysis of the samples.

Results and Discussion

X-Ray Diffraction (XRD)

The XRD patterns acquired for pure V_2O_5, SVO, and irradiated SVO were analysed. The diffraction peaks of pure V_2O_5 matched with JCPDS card no. 00-001-0359, confirming an orthorhombic crystalline phase[42] (Fig 1b). The diffraction peaks appeared at $2\theta = 15.53°$, 20.25°, 21.71°, 26.26°, 31.13°, 32.41°, 34.33°, 41.30°, and 51.59° for lattice planes (200), (010), (110), (101), (400), (011), (301), (020), and (221). In the diffraction pattern obtained for SVO, the peak position of the lattice plane (010) was found to shift towards the lower 2θ value (Fig. 1a). The dopant tin (Sn) atom, with an atomic radius of 140 pm, is greater than the vanadium (V) atom, having an atomic radius of 134 pm. The presence of Sn atoms induces localized stress within the lattice. This results in lattice expansion, leading to an increase in interplanar spacing. This causes variations in lattice parameters and ultimately leads to a shift in the position of diffraction peaks.[26,43,44]

A comparative analysis of XRD patterns revealed a significant structural alteration of SVO after SHI irradiation. An XRD peak with elevated background noise and lower peak intensity for irradiated SVO suggests a disruption of periodicity and a more disordered crystal lattice. A phase transformation was observed post-irradiation, caused by the emergence of a new phase V_4O_9 (JCPDS card no. 00-023-0720).[45] V_4O_9 possesses a tetragonal crystal symmetry having space group P42/mnm (Fig. 1c). The lattice parameters are $a = 8.23$ Å, $b = 8.23$ Å, and $c = 10.32$ Å, respectively, at $\alpha = \beta = \gamma = 90°$. In Fig. 1d, e, and f, the correlation between the full width at half maximum (FWHM) ($\beta \cos\theta$) and diffraction angle ($4 \sin\theta$) is presented for SVO and irradiated SVO. The positive slope obtained indicates an increase in tensile strain post-irradiation. The calculation of crystallite size, performed using the Debye–Scherrer (Eq. 1) and the Williamson–Hall W-H methods (Eq. 2), revealed a reduction in crystallite size post-irradiation[46] (Table I).

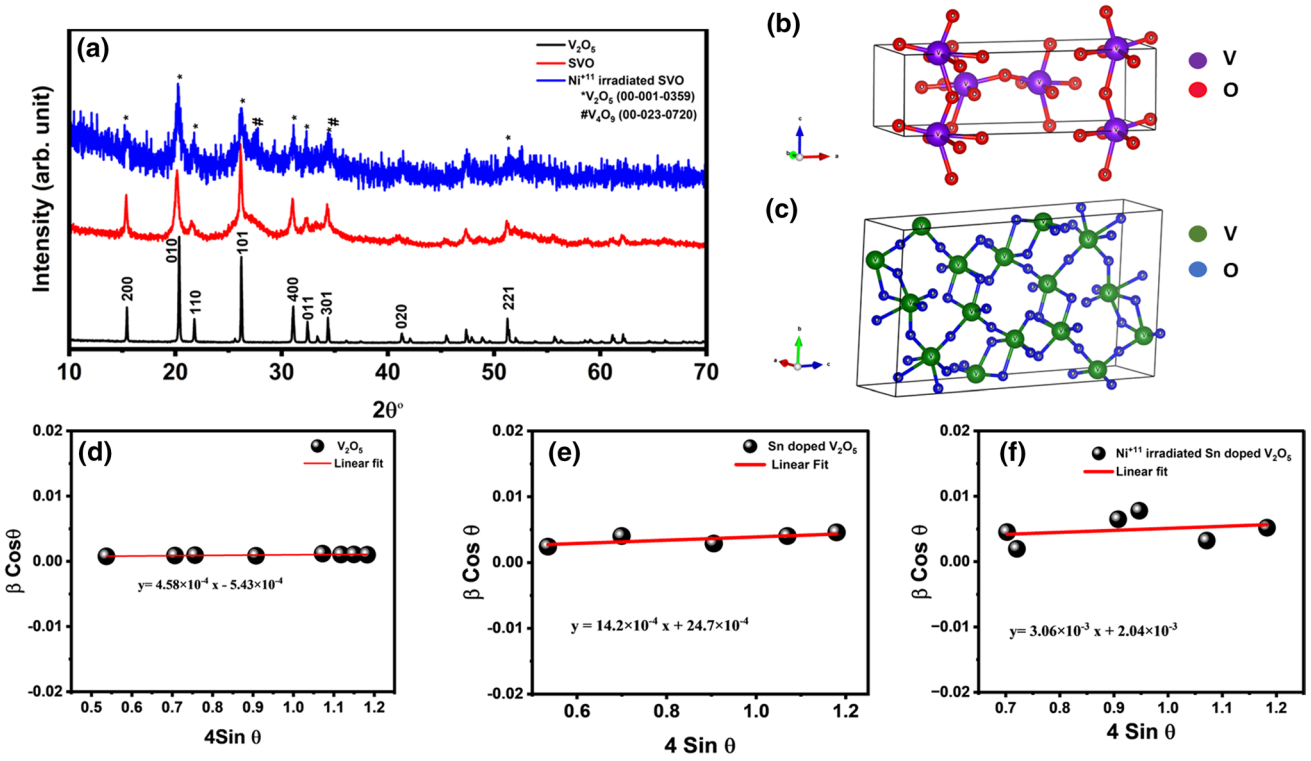

Fig. 1 (a) XRD spectra of V_2O_5, pristine SVO, and irradiated SVO. Crystal structure of (b) V_2O_5 and (c) V_4O_9. W-H plot for (d) V_2O_5, (e) pristine SVO, and (f) irradiated SVO.

$$D = \frac{K\lambda}{\beta \cos\theta}, \tag{1}$$

Table 1 Structural parameters of V_2O_5, pristine SVO, and irradiated SVO

Sample	Strain	Crystallite size	
		D_{DS}	D_{WH}
V_2O_5	4.58×10^{-4}	23.14 nm	25.00 nm
Pristine SVO	14.2×10^{-4}	46.31 nm	17.55 nm
Irradiated SVO	30.6×10^{-4}	29.95 nm	14.27 nm

$$\beta \cos\theta = \frac{K\lambda}{D} + 4\epsilon\lambda \sin\theta, \tag{2}$$

where the crystallite size, x-ray wavelength, Scherrer constant, FWHM, Bragg angle, and lattice strain are denoted by D, λ, K (0.9), β, Θ, and ϵ, respectively.

Field-Emission Scanning Microscopy (FESEM)

FESEM images for pure V_2O_5, SVO, and irradiated SVO were obtained at a resolution of micrometres (Fig. 2a, b, and c, respectively). The images of the irradiated SVO reveal more textured morphology characterized by fine lines and

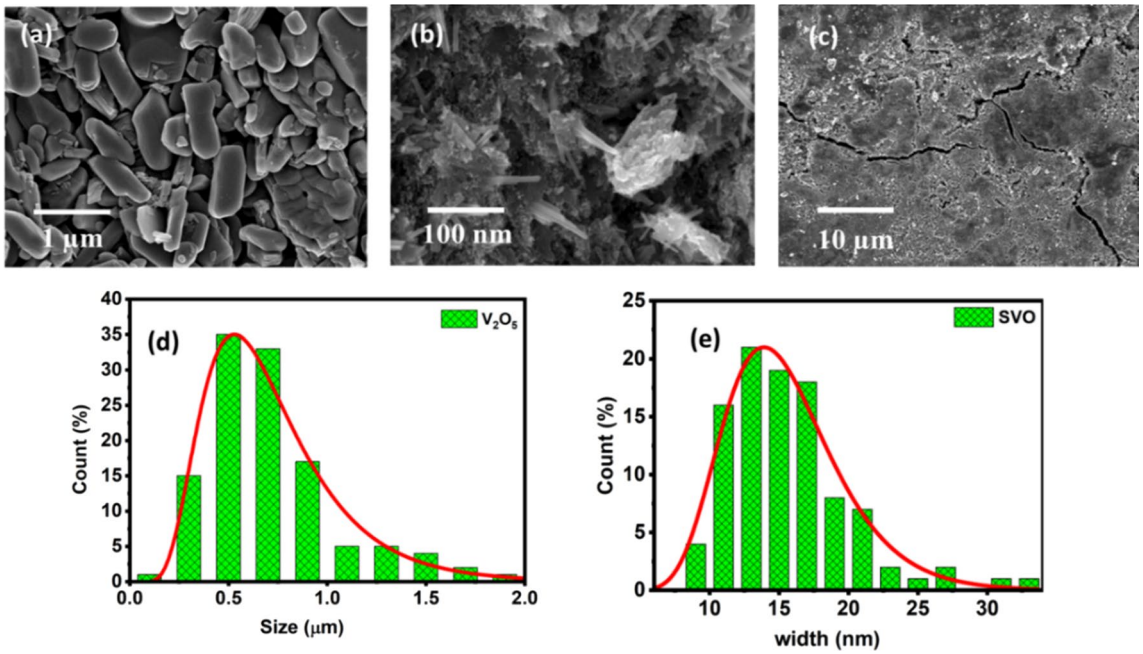

Fig. 2 FESEM images of (a) V_2O_5, (b) pristine SVO, (c) irradiated SVO. Grain size distribution of (d) V_2O_5 and (e) pristine SVO nanobelts.

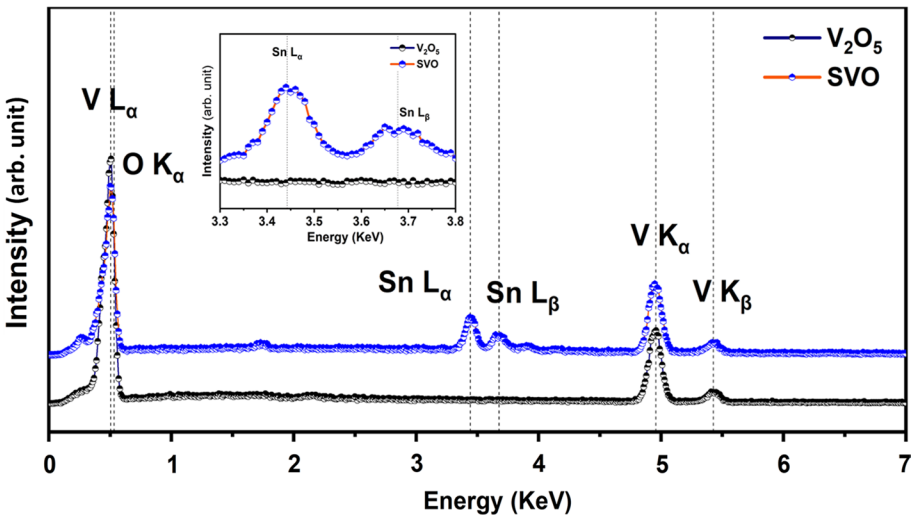

Fig. 3 EDX spectrum for V_2O_5 and pristine SVO; characteristic peaks of Sn are shown in the inset.

cracks.[47] A crystallite size distribution curve was obtained for V_2O_5 and SVO (Fig. 2d and e, respectively). For doping confirmation, a comparative plot of the energy-dispersive x-ray (EDX) spectrum of V_2O_5 and SVO was obtained, revealing the characteristic peaks of constituent elements (Fig. 3). Two new peaks of L_α and L_β spectral lines appeared at 3.44 keV and 3.66 keV in SVO, confirming the existence of Sn in SVO. Weight percentages of 13.0%, 63.1%, and 23.9% were found for oxygen (O), vanadium (V), and tin (Sn) atoms, respectively; the atomic percentages were 36.1%, 55%, and 8.9%, respectively (Table II).

An essential condition with the thermal spike model is a rapid cooldown after irradiation to effectively preserve the alterations induced by intense heating.[2] In this study, SVO did not undergo quenching. Also, due to the lack of substantial evidence confirming the melting in SVO when subjected to SHI irradiation, the adequacy of the thermal spike model in accurately illustrating surface modifications remains uncertain.[48] This model overlooks the transformative capacity of the lattice relaxation stage. As emphasized by the bond weakening model, an intense electronic excitation induces variations in interatomic interactions, resulting in lattice relaxation.

In the irradiated SVO, the intense excitation of bonding electrons leads to the disturbance of lattice order, initiating structural modifications during lattice relaxation.[9,49] The induced alterations are carried to or annealed in the heating stage.[50] Heating leads to thermal expansion following contractions as atoms conduct heat to the surrounding lattice. The resulting thermal stress causes cracks as the material adjusts to the temperature change. The SVO transforms from a crystalline to an amorphous state post-irradiation. The amorphized SVO sample is expected to exhibit differing physical and chemical properties.[51] We propose that the modified morphology is a product of processes set in motion during both the lattice relaxation and heating stages.

Table II EDX results for pristine SVO

Element	Weight%	Atomic%
O K	13.0	36.1
V K	63.1	55.0
Sn L	23.9	8.9

Atomic Force Microscopy (AFM)

AFM images of pure V_2O_5, SVO, and irradiated SVO are depicted in Fig. 4a, b, and c, respectively. AFM images were acquired to examine the microscale features and topographical variations induced by the irradiation process. Amplitude parameters were quantitively analysed for the surface profile, wherein the average roughness and root mean square (RMS) roughness denoted by (R_a) and (R_q), respectively, were observed to increase post-irradiation. Average roughness of 81.760 nm and 125.846 nm was calculated for the pristine and irradiated samples, respectively. The RMS roughness takes into account both the magnitude and direction of surface features and was calculated as 104.544 nm and 163.085 nm for SVO and irradiated SVO, respectively. The roughness ratio was found to be 0.64. In the pristine sample, the highest peak (R_p) and deepest valley (R_v) were quantified in the order of nanometres (10^{-9}). Following irradiation, these measurements increased to the order of micrometres (10^{-6})[52–54] (Table III).

UV–Visible Spectroscopy

To better understand the electronic transitions occurring within the material, UV–visible absorption spectra were acquired for V_2O_5, SVO, and irradiated SVO samples. The doping of Sn in V_2O_5 results in crystal defects such as oxygen vacancies that trap excited electrons, causing the absorption edge to shift towards a longer wavelength, leading to a reduction in the bandgap.[55] In the case of SVO, the absorption peak occurring at 500 nm is attributed to the π–π^* transition.[56,57] Upon Ni^{+11} irradiation, the peak shifted to a lower wavelength region, approximately 420 nm, signifying a modification in the electronic band structure (Fig. 5a). The material's bandgap plays a pivotal role in determining its optical and electronic properties. The bandgap, calculated using the Kubelka–Munk function (Eq. 3), indicates an increase from 1.65 eV to 1.82 eV

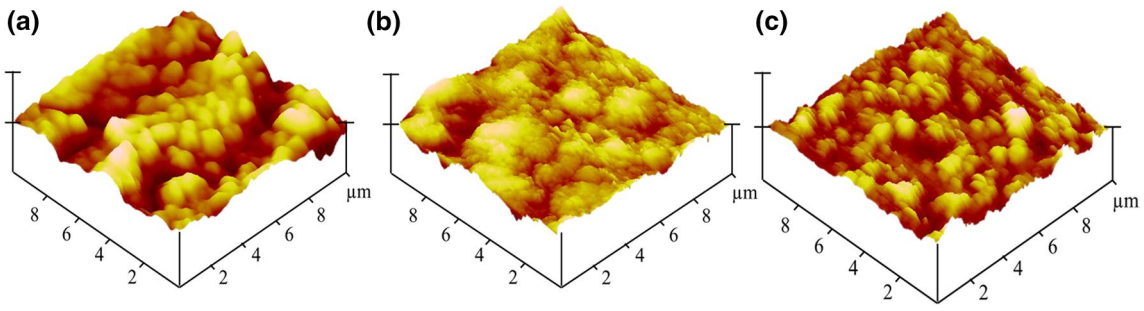

Fig. 4 AFM image of (a) V_2O_5, (b) pristine SVO, and (c) irradiated SVO.

post-irradiation[58] (Table IV). Observed modification in bandgap indicates a shift in energy levels and electronic density of states, and potential modification in charge carrier behaviour. V_4O_9 has a large bandgap relative to V_2O_5.[59] The bandgap variation is possibly due to the formation of the V_4O_9 phase. Also, amorphous materials formed post-irradiation lack long-range periodicity, which can lead to localized electronic states wherein the electrons have limited mobility and are confined to smaller regions. This hinders the movement of electrons between the valence and conduction bands. The bandgap increases, as electrons now require additional energy to overcome these barriers for transition between bands. The transformed material is suitable for numerous applications including photodetectors,[60] solar cells,[61] and sensors.[62]

$$[F(R\infty) \times hv]^n = A(hv - E_g), \tag{3}$$

where $F(R_\infty)$ and R_∞ denote the Kubelka–Munk function and the reflectance of the material with respect to the buffer solution used as a reference, for indirect-bandgap $n = \frac{1}{2}$.

Fourier Transform Infrared Spectroscopy (FTIR)

The infrared (IR) spectra of SVO and irradiated SVO samples are shown in Fig. 6. Some bending and stretching vibration peaks were observed in the fingerprint region, as tabulated in Table V).[63,64] The bands of V=O and V–O–V asymmetric stretching are the signature peaks of vanadium oxides. The peak of V=O emerged at 1017.64 cm^{-1}, 1014.91 cm^{-1}, and 994.53 cm^{-1} in pure V_2O_5, pristine SVO, and irradiated SVO, respectively. The peaks of V=O and V–O–V appeared at approximately the same position due to the presence of V_2O_5. In irradiated SVO, a peak broadening was observed due to the cumulative peak of V_2O_5 and V_4O_9.[65] This demonstrates the formation of the V_4O_9 phase in the material. The peak of V–O–V symmetric stretching was observed in pure V_2O_5 and SVO samples and was found to disappear in irradiated SVO, revealing that symmetric vibrations were forbidden in the damaged lattice plane. The sharp peaks of O–Sn–O bending are indicative of well-defined and localized band vibrations in SVO samples. The peak shifting in the fingerprint region indicates a change in the vibrational energy of the involved molecular bonds. The bending modes of V–O–V were found to shift towards lower wavenumbers post-irradiation, indicating that the interaction with Ni ions causes an increase in molecular mass.[66,67] The structural modifications and decrease in bond length are induced by Ni^{+11} ion bombardment.

Table III Height parameters of V_2O_5, pristine SVO, and irradiated SVO

Parameters	R_a	R_q	R_p	R_v
V_2O_5	17.264 nm	23.474 nm	121.174 nm	142.205 nm
Pristine SVO	81.760 nm	104.544 nm	481.580 nm	511.169 nm
Irradiated SVO	125.846 nm	163.085 nm	0.94484 µm	0.76383 µm

Conclusions

This detailed characterization provides insights into the structural, electronic, and chemical variations induced by the irradiation of Ni^{+11} ions on SVO. The Sn doping in V_2O_5 was confirmed by the increase in the tensile strain as revealed by XRD and from the characteristic peaks of constituent elements obtained by the EDX spectrum. The emergence of a new phase V_4O_9, increase in tensile strain, and decrease in crystallite size suggest structural alterations induced by irradiation. AFM and FESEM analysis revealed increases in surface roughness and a textured morphology with fine lines and cracks post-irradiation.

Table IV Bandgap calculated using Tauc plot for V_2O_5, pristine SVO, and irradiated SVO

Sample	V_2O_5	SVO	Irradiated SVO
Bandgap (eV)	2.1	1.65	1.82

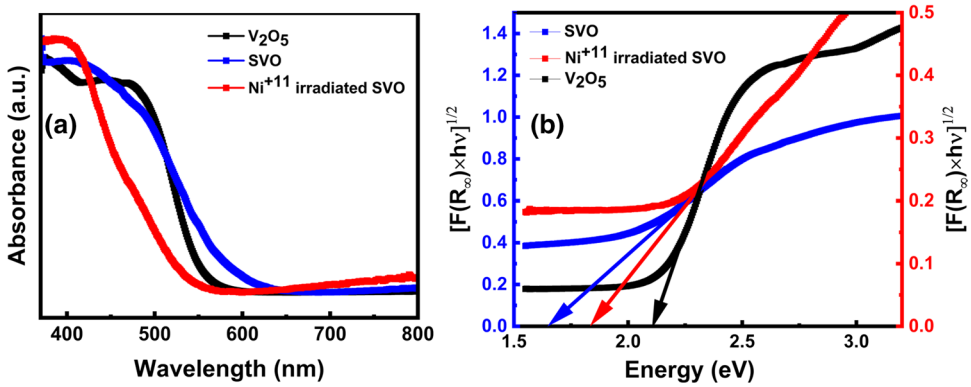

Fig. 5 (a) Absorption spectra of V_2O_5, pristine SVO, and irradiated SVO. (b) Graph of $[F(R_\infty) \times hv]^{1/2}$ versus energy for V_2O_5, pristine SVO, and irradiated SVO.

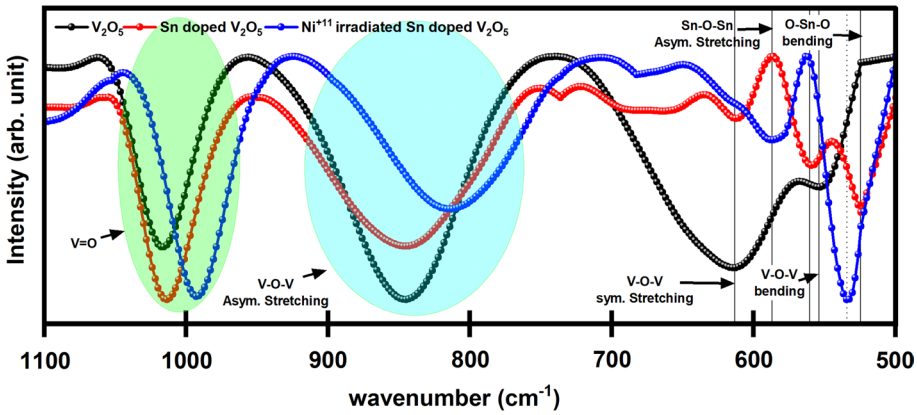

Fig. 6 FTIR spectra of V_2O_5, pristine SVO, and irradiated SVO.

Table V Vibrations and bond positions of pristine SVO and irradiated SVO samples with respective wavenumbers (cm^{-1})

Bond/vibrations	Pristine SVO	Ni^{+11}-irradiated SVO
V–O–V bending	553.21	587.06
V–O–V asymmetric stretching	846.04	815.61
V=O	1013.5	992.53
Sn–O–Sn asymmetric	608.00	608.00
O–Sn–O bending	524.06	533.48

The induced modifications are a result of the lattice relaxation and heating stage, where the alterations generated in the relaxation stage are carried to and annealed in the heating stage. The cracks and fine lines result from stress induced as the material adjusts to temperature changes. UV–visible spectra revealed a blue shift in the absorption peak, and the electronic bandgap increased from 1.65 eV to 1.82 eV post-irradiation, suggesting a potential modification in charge carrier behaviour. This results from the formation of a new phase V_4O_9 having a higher bandgap and the amorphous state of the material obtained post-irradiation. FTIR analysis revealed a peak shift in the fingerprint region, indicating a change in the vibrational energy of the involved molecular bonds.

This comprehensive study provides insights into the mechanisms governing the enhanced physiochemical characteristics caused by SHI irradiation. The combined results suggest that Ni^{+11} irradiation alters the material's lattice parameters, crystallite size, surface morphology, and electronic band structure. The modified material holds the potential for utilization in electronic applications, as it is expected to show enhanced results in detecting ammonia gases and to be suitable for use in lithium-ion batteries. Hence, testing this material for increased efficiency is an objective of future research.

Acknowledgments The authors would like to express special thanks to the Sophisticated Analytical Instrument Facility (SAIF) and Central Analytical Facilities (CAF), Manipal University Jaipur, for the provisions of FESEM, XRD, UV-Vis, and FTIR facilities, respectively, for characterization. RN would like to acknowledge the Inter-University Accelerator Center, New Delhi for providing swift heavy ion beam facilities. RN acknowledges the award of the Enhanced Seed Grant Project No. EF/2019-21/QE04-03 to her at Manipal University Jaipur, Jaipur. SSR would like to acknowledge the Science and Engineering Research Board (SERB), Govt. of India for financial support under sanctioned project no. ECR/2017/002691.

Data Availability Data will be made available on reasonable request.

Conflict of interest The authors declare that they have no known competing financial interests or personal relationships that could have appeared to influence the work reported in this paper.

References

1. C. Dufour and M. Toulemonde, Models for the description of track formation. *Ion Beam Modif. Solids Ion-Solid Interact. Radiat. Damage* 61, 63 (2016).
2. N. Itoh, D. Duffy, S. Khakshouri, and A. Stoneham, Making tracks: electronic excitation roles in forming swift heavy ion tracks. *J. Phys. Condens. Matter* 21(47), 474205 (2009).
3. E. Bringa and R. Johnson, Coulomb explosion and thermal spikes. *Phys. Rev. Lett.* 88(16), 165501 (2002).
4. A. Abdullaev, K. Sekerbayev, R. Rymzhanov, V. Skuratov, J.O. Connell, B. Shukirgaliyev, A. Kozlovskiy, Y. Wang, and Z. Utegulov, Impact of swift heavy ion-induced point defects on nanoscale thermal transport in zno. *Mater. Res. Bull.* 175, 112786 (2024).
5. R. Darkins and D.M. Duffy, Modelling radiation effects in solids with two-temperature molecular dynamics. *Comput. Mater. Sci.* 147, 145 (2018).
6. O. Osmani, I. Alzaher, T. Peters, B.B. d'Etat, A. Cassimi, H. Lebius, I. Monnet, N. Medvedev, B. Rethfeld, and M. Schleberger, Damage in crystalline silicon by swift heavy ion irradiation. *Nucl. Instrum. Methods Phys. Res. Sect. B* 282, 43 (2012).
7. N. Szymanski, Z. Liu, T. Alderson, N. Podraza, P. Sarin, and S. Khare, Electronic and optical properties of vanadium oxides from first principles. *Comput. Mater. Sci.* 146, 310 (2018).
8. M. Balaji, M.M. Raja, K. Asokan, D. Kanjilal, T. Rajasekaran, and D.P. Padiyan, Effect of thermal spike energy created in $CuFe_2O_4$

by 150 MeV Ni11+ swift heavy ion irradiation. *Nucl. Instrum. Methods Phys. Res. Sect. B* 269(10), 1088 (2011).
9. D.R. Rittman, C.L. Tracy, A.B. Cusick, M.J. Abere, B. Torralva, R.C. Ewing, and S.M. Yalisove, Ultrafast laser and swift heavy ion irradiation: response of Gd_2O_3 and ZrO_2 to intense electronic excitation. *Appl. Phys. Lett.* 106(17), 171914 (2015).
10. F. Agullo-Lopez, A. Climent-Font, A. Munoz-Martin, and A. Zucchiatti, Alternative approaches to electronic damage by ion-beam irradiation: exciton models. *Phys. Status Solidi A* 213(11), 2960 (2016).
11. H. Brooks, Radiation effects in materials. *J. Appl. Phys.* 30(8), 1118 (1959).
12. V. Chauhan, D. Gupta, N. Koratkar, and R. Kumar, Phase transformation and enhanced blue photoluminescence of zirconium oxide poly-crystalline thin film induced by ni ion beam irradiation. *Sci. Rep.* 11(1), 17672 (2021).
13. D. Kanjilal, Swift heavy ion-induced modification and track formation in materials. *Curr. Sci.* 80, 1560 (2001).
14. K. Gupta, S. Kumar, and R. Singhal, Phase transformation by the irradiation with swift heavy ions on vanadium oxide thin films. *Radiat. Eff. Defects Solids* 175(5–6), 450 (2020).
15. Z. Aftab, I. Sulania, A. Kandasami, and L. Nair, Swift heavy ion-induced reactivity and surface modifications in indium thin films. *ACS Omega* 7(36), 31869 (2022).
16. S.F. Cogan, N.M. Nguyen, S.J. Perrotti, and R.D. Rauh, Optical properties of electrochromic vanadium pentoxide. *J. Appl. Phys.* 66(3), 1333 (1989).
17. Y. Wei, J. Zhou, J. Zheng, and C. Xu, Improved stability of electrochromic devices using Ti-doped V_2O_5 film. *Electrochim. Acta* 166, 277 (2015).
18. S.H. Kim, J.S. Cha, Y.S. Jeon, B.C. Park, M.-C. Shin, J.-K. Song, and Y.K. Kim, Catalytic activity of vanadium oxide catalysts prepared by electrodeposition for the selective catalytic reduction of nitrogen oxides with ammonia. *React. Kinet. Mech. Catal.* 118, 633 (2016).
19. C. Wu and Y. Xie, Promising vanadium oxide and hydroxide nanostructures: from energy storage to energy saving. *Energy Environ. Sci.* 3(9), 1191 (2010).
20. K. Schneider, M. Lubecka, and A. Czapla, V_2O_5 thin films for gas sensor applications. *Sens. Actuat. B Chem.* 236, 970 (2016).
21. S. Dhall, N. Jaggi, and R. Nathawat, Functionalized multiwalled carbon nanotubes based hydrogen gas sensor. *Sens. Actuat. A Phys.* 201, 321 (2013).
22. B. Ahmad and P.K. Ahmad, Thermophysical properties of silver doped V_2O_5 thin films. *Russ. J. Appl. Chem.* 4, 599 (2017).
23. K. Jeyalakshmi, Electrochemical behavior of tin doped vanadium pentoxide thin films. *Int. J. Res. Pharmaceut. Sci.* 7, 282 (2016).
24. V.K. Sharma, A.K. Kumawat, S.S. Rathore, I. Sulania, R. Meena, S. Kedia, and D.R. Nathawat, The shi irradiation induced transition to negative dielectric constant phase in K2Bi4Ti4WO18. *Front. Phys.* 11, 1127118 (2023).
25. R. Mohan, P. Manimuthu, C. Venkateswaran, A. Sendilkumar, and K. Asokan, 200 Mev Ag^{15+} ion beam irradiation effects on spray deposited 5 wt.% 'Li' doped V_2O_5 thin film. in AIP Conference Proceedings, vol. 1731 (2016).
26. C. Yan and L. Liu, Sn-doped V_2O_5 nanoparticles as catalyst for fast removal of ammonia in air via pec and pec-mfc. *Chem. Eng. J.* 392, 123738 (2020).
27. N. Singh, A. Umar, N. Singh, H. Fouad, O.Y. Alothman, and F.Z. Haque, Highly sensitive optical ammonia gas sensor based on sn doped V_2O_5 nanoparticles. *Mater. Res. Bull.* 108, 266 (2018).
28. Z. Li, C. Zhang, C. Liu, H. Fu, X. Nan, K. Wang, X. Li, W. Ma, X. Lu, and G. Cao, Enhanced electrochemical properties of Sn-doped V_2O_5 as a cathode material for lithium ion batteries. *Electrochim. Acta* 222, 1831 (2016).
29. Y. Li, J. Yao, E. Uchaker, M. Zhang, J. Tian, X. Liu, and G. Cao, Sn-doped V_2O_5 film with enhanced lithium-ion storage performance. *J. Phys. Chem. C* 117(45), 23507 (2013).
30. S. Le, Y. Li, S. Xiao, T. Sun, J. Yao, and Z. Zou, Enhanced reversible lithium storage property of $Sn_{0.1}V_2O_5$ in the voltage window of 1.5–4.0 V. *Solid State Ionics* 341, 115028 (2019).
31. Z. Yuan, R. Li, F. Meng, J. Zhang, K. Zuo, and E. Han, Approaches to enhancing gas sensing properties: a review. *Sensors* 19(7), 1495 (2019).
32. Y. Qi, G. Wang, S. Li, T. Liu, J. Qiu, and H. Li, Recent progress of structural designs of silicon for performance-enhanced lithium-ion batteries. *Chem. Eng. J.* 397, 125380 (2020).
33. Z. Chen, Q. Zhang, and Q. Liang, Carbon-coatings improve performance of Li-ion battery. *Nanomaterials* 12(11), 1936 (2022).
34. J. Zheng, J. Lu, K. Amine, and F. Pan, Depolarization effect to enhance the performance of lithium ions batteries. *Nano Energy* 33, 497 (2017).
35. D. Dalavi, N. Harale, I. Mulla, V. Rao, V. Patil, I. Kim, J. Kim, and P. Patil, Nanoporous network of nickel oxide for ammonia gas detection. *Mater. Lett.* 146, 103 (2015).
36. J. Cao, Z. Wang, R. Wang, S. Liu, T. Fei, L. Wang, and T. Zhang, Synthesis of core–shell α-Fe_2O_3@nionanofibers with hollow structures and their enhanced hcho sensing properties. *J. Mater. Chem. A* 3(10), 5635 (2015).
37. X. Zeng, C. Zhan, J. Lu, and K. Amine, Stabilization of a high-capacity and high-power nickel-based cathode for li-ion batteries. *Chem* 4(4), 690 (2018).
38. Y. Ding, D. Mu, B. Wu, R. Wang, Z. Zhao, and F. Wu, Recent progresses on nickel-rich layered oxide positive electrode materials used in lithium-ion batteries for electric vehicles. *Appl. Energy* 195, 586 (2017).
39. J. Pan, C. Li, Y. Peng, L. Wang, B. Li, G. Zheng, and M. Song, Application of transition metal (Ni, Co and Zn) oxides based electrode materials for ion-batteries and supercapacitors. *Int. J. Electrochem. Sci*. 100233 (2023).
40. D. Bokov, A. Turki Jalil, S. Chupradit, W. Suksatan, M. Javed Ansari, I.H. Shewael, G.H. Valiev, and E. Kianfar, Nanomaterial by sol–gel method: synthesis and application. *Adv. Mater. Sci. Eng.* 2021, 1 (2021).
41. S. Som, S. Das, S. Dutta, M.K. Pandey, R.K. Dubey, H. Visser, S. Sharma, and S. Lochab, A comparative study on the influence of 150 Mev Ni^{7+}, 120 Mev Ag^{9+}, and 110 Mev Au^{8+} swift heavy ions on the structural and thermolu- minescence properties of Y_2O_3: Eu3+/Tb3+ nanophosphor for dosimetric applications. *J. Mater. Sci.* 51, 1278 (2016).
42. T.K. Le, M. Kang, and S.W. Kim, A review on the optical characterization of V_2O_5 micro-nanostructures. *Ceram. Int.* 45(13), 15781 (2019).
43. V. Modafferi, G. Panzera, A. Donato, P. Antonucci, C. Cannilla, N. Donato, D. Spadaro, and G. Neri, Highly sensitive ammonia resistive sensor based on electrospun V_2O_5 fibers. *Sens. Actuat. B Chem.* 163(1), 61 (2012).
44. D. Govindarajan, R. Gopalakrishnan, T. Maiyalagan et al., RGO-encapsulated Sn-doped V_2O_5 nanorods for high-performance supercapacitors. *Mater. Today Commun.* 27, 102357 (2021).
45. K.-A. Wilhelmi and K. Waltersson, On the crystal structure of a new vanadium oxide, V_4O_9. *Acta Chem. Scand.* 24(19), 3409 (1970).
46. A.K. Kumawat, S.S. Rathore, S. Singh, and R. Nathawat, Structural transition and photoluminescence behavior of (V_2O_5) 1–x $(Ag_{0.33}V_2O_5)$ x (x = 0 to 01) nanocomposites. *Results Chem.* 5, 100802 (2023).
47. C.L. Tracy, M. Lang, J. Zhang, F. Zhang, Z. Wang, and R.C. Ewing, Structural response of A_2TiO_5 (A = La, Nd, Sm, Gd) to swift heavy ion irradiation. *Acta Mater.* 60(11), 4477 (2012).

48. W. Wesch, A. Kamarou, and E. Wendler, Effect of high electronic energy deposition in semiconductors. *Nucl. Instrum. Methods Phys. Res. Sect. B* 225(1–2), 111 (2004).
49. W. Wesch, A. Kamarou, E. Wendler, A. Undisz, and M. Rettenmayr, Effect of high electronic excitation in swift heavy ion irradiated semiconductors. *Nucl. Instrum. Methods Phys. Res. Sect. B* 257(1–2), 283 (2007).
50. R. Nathawat, A.K. Kumawat, S.S. Rathore, A.K. Mukhopadhyay, and K. Kabra, Effect of heat treatment on band gap of V_2O_5. *J. Nano Electron. Phys*. 13(1), 01030 (2021).
51. A.B. Cusick, M. Lang, F. Zhang, K. Sun, W. Li, P. Kluth, C. Trautmann, and R.C. Ewing, Amorphization of Ta_2O_5 under swift heavy ion irradiation. *Nucl. Instrum. Methods Phys. Res. Sect. B* 407, 25 (2017).
52. M. Kwoka, L. Ottaviano, and J. Szuber, AFM study of the surface morphology of L-CVD SnO_2 thin films. *Thin Solid Films* 515(23), 8328 (2007).
53. D. Rugar and P. Hansma, Atomic force microscopy. *Phys. Today* 43(10), 23 (1990).
54. M.K. Jaiswal, A. Kumar, D. Kanjilal, and T. Mohanty, Swift heavy ion induced topography changes of tin oxide thin films. *Appl. Surf. Sci.* 263, 586 (2012).
55. D.O. Scanlon, A. Walsh, B.J. Morgan, and G.W. Watson, An ab initio study of reduction of V_2O_5 through the formation of oxygen vacancies and Li intercalation. *J. Phys. Chem. C* 112(26), 9903 (2008).
56. J. Parker, D. Lam, Y.-N. Xu, and W. Ching, Optical properties of vanadium pentoxide determined from ellipsometry and band-structure calculations. *Phys. Rev. B* 42(8), 5289 (1990).
57. A.K. Kumawat, R. Nathawat, S.S. Rathore, and A.K. Mukhopadhyay, Band gap tuning possibilities in vanadium oxide. *Mater. Today Proc.* 43, 2939 (2021).
58. M.L. Myrick, M.N. Simcock, M. Baranowski, H. Brooke, S.L. Morgan, and J.N. McCutcheon, The Kubelka-Munk diffuse reflectance formula revisited. *Appl. Spectrosc. Rev.* 46(2), 140 (2011).
59. M. Chine, F. Sediri, and N. Gharbi, Solvothermal synthesis of V_4O_9 flake-like morphology and its photocatalytic application in the degradation of methylene blue. *Mater. Res. Bull.* 47(11), 3422 (2012).
60. M. Singh, G. Kumar, N. Prakash, S.P. Khanna, P. Pal, and S.P. Singh, Large bandgap reduced graphene oxide (RGO) based n-p+ heterojunction photodetector with improved nir performance. *Semicond. Sci. Technol.* 33(4), 045012 (2018).
61. Y. Zhao and K. Zhu, Efficient planar perovskite solar cells based on 1.8 eV band gap $CH_3NH_3PbI_2Br$ nanosheets via thermal decomposition. *J. Am. Chem. Soc.* 136(35), 12241 (2014).
62. D.K. Maurya, S. Sikarwar, P. Chaudhary, S. Angaiah, and B.C. Yadav, Synthesis and characterization of nanostructured copper zinc tin sulphide (CZTS) for humidity sensing applications. *IEEE Sens. J.* 19(8), 2837 (2019).
63. A.B.D. Nandiyanto, R. Oktiani, and R. Ragadhita, How to read and interpret ftir spectroscope of organic material. *Indones. J. Sci. Technol.* 4(1), 97 (2019).
64. F.A. Sabah, I.A. Razak, E. Kabaa, M. Zaini, and A. Omar, Characterization of hybrid organic/inorganic semiconductor materials for potential light emitting applications. *Opt. Mater.* 107, 110117 (2020).
65. Q. Wang, T. Sun, S. Zheng, L. Li, T. Ma, and J. Liang, A new tunnel-type V_4O_9 cathode for high power density aqueous zinc ion batteries. *Inorgan. Chem. Front.* 8(20), 4497 (2021).
66. K. Shafeeq, V. Athira, C.R. Kishor, and P. Aneesh, Structural and optical properties of V_2O_5 nanostructures grown by thermal decomposition technique. *Appl. Phys. A* 126, 1 (2020).
67. M. Boronat, P. Concepcion, A. Corma, M. Renz, and S. Valencia, Determination of the catalytically active oxidation lewis acid sites in sn-beta zeolites, and their optimisation by the combination of theoretical and experimental studies. *J. Catal.* 234(1), 111 (2005).